electronics

MDPI

Article

Investigation of Ring-Shaped TENG for Optoelectronic Information Communication

Dongxin Yang [1,2,3], Jingming Wang [2,*], Manyun Zhang [3], Hao Li [3], Liu Wang [1,*], Rui Yuan [3,*] and Zhiyuan Zhu [3,*]

[1] Key Laboratory of Intelligent Rehabilitation and Barrier-free for the Disabled, Changchun University, Ministry of Education, Changchun 130022, China
[2] School of Mechanical and Electrical Engineering, Chuzhou University, Chuzhou 239012, China
[3] College of Electronic and Information Engineering, Southwest University, Chongqing 400715, China
* Correspondence: wjmtime@chzu.edu.cn (J.W.); wangl95@ccu.edu.cn (L.W.); yuanruiswu@swu.edu.cn (R.Y.); zyuanzhu@swu.edu.cn (Z.Z.)

Abstract

With the advancement of smart management technologies, research on self-powered silicon PIN photodetectors has become increasingly important. In this paper, a triboelectric nanogenerator (TENG)-driven silicon PIN photodetector based on power management circuitry is proposed. Through rectification and filtering, the pulse signal from the TENG is converted into stable DC voltage, providing reverse bias for the photodetector. With a 5 MΩ sampling resistor, the system generates a voltage of 0.4 V in the absence of light, which gradually increases to 7.3 V and saturates as the light intensity increases to 300 Lux, demonstrating good compatibility and near independence from the TENG rotation speed. Additionally, a light communication system is constructed, with the TENG-driven silicon PIN photodetector as the receiver unit and a signal transmission unit consisting of a finger-pressed TENG combined with an LED. This system successfully transmits Morse code signals such as "SOS" and "TENG".

Keywords: triboelectric nanogenerator; TENG-powered sensing; photoelectric detection

1. Introduction

With the rise of the Internet of Things (IoT) era [1], billions of sensors have enabled diverse applications such as environmental monitoring, industrial production, equipment surveillance, and the advancement of smart city projects. P-I-N structured photodetectors [2–8] utilize semiconductor materials and established fabrication processes, providing several advantages such as compact size, lightweight design, shock resistance, high efficiency, low power consumption, and long lifespan [9–14]. As a result, they are extensively employed in optical fields, including infrared imaging, LIDAR, and communication systems. Recent research has also investigated novel materials and structures, such as graphene-based photodetectors [15,16] and infrared detectors featuring optically tunable barriers [17,18], aimed at enhancing sensitivity and overall performance. However, silicon PIN detectors must operate in a fully depleted state, where the full depletion voltage (FDV) is critical for effectively collecting electron-hole pairs generated by ionization. As the thickness of the detector increases, the required operating voltage can escalate to kilovolt levels, posing significant challenges for conventional high-voltage power sources. Traditional power supplies are often expensive, difficult to recycle, environmentally harmful, and frequently inadequate for meeting high-voltage demands. Consequently, there is a pressing need to develop alternative powering methods to address these challenges.

Check for updates

Academic Editor: José Matas

Received: 21 November 2025
Revised: 18 December 2025
Accepted: 23 December 2025
Published: 29 December 2025

Copyright: © 2025 by the authors. Licensee MDPI, Basel, Switzerland. This article is an open access article distributed under the terms and conditions of the Creative Commons Attribution (CC BY) license.

By combining the effects of contact electrification and electrostatic induction, TENGs can effectively convert mechanical energy into electric power or signals [19]. Typically, when two dissimilar materials come into contact, surface triboelectric charges are generated. Subsequent mechanical motion-induced separation or sliding between these materials disturbs the electrostatic equilibrium, driving the flow of electrons through an external circuit to generate alternating current. Based on the configuration of the electrodes and the type of mechanical excitation, TENGs primarily operate in four fundamental modes (Figure 1): vertical contact-separation, lateral sliding, single-electrode, and freestanding triboelectric-layer modes [20,21]. However, the instability of TENG's output is a major issue for TENG-based photodetector systems, as reliable operation requires stable and sensitive performance. Despite this problem, Wang et al. conducted groundbreaking research in 2012 and advanced a significant amount of work in the application field of TENG [22–24]. Studies have shown various uses of TENG, including micro- and nano-energy harvesting [25], TENG-driven sensors [26,27], blue energy harvesting [28,29], and high-voltage power sources [30]. The sustainability and high-voltage output of TENG have attracted widespread attention [31–35]. Many applications have been realized through the TENG mechanism, such as pressure sensors [36,37], vibration sensors [38,39], wind speed sensors [40,41], and gas sensors [42,43]. Therefore, improving the consistency and stability of TENG output is crucial for enhancing the overall reliability of silicon PIN detectors in harsh environments. This not only helps improve the performance of TENG-driven photodetectors but also facilitates their wider application in various critical Internet of Things scenarios.

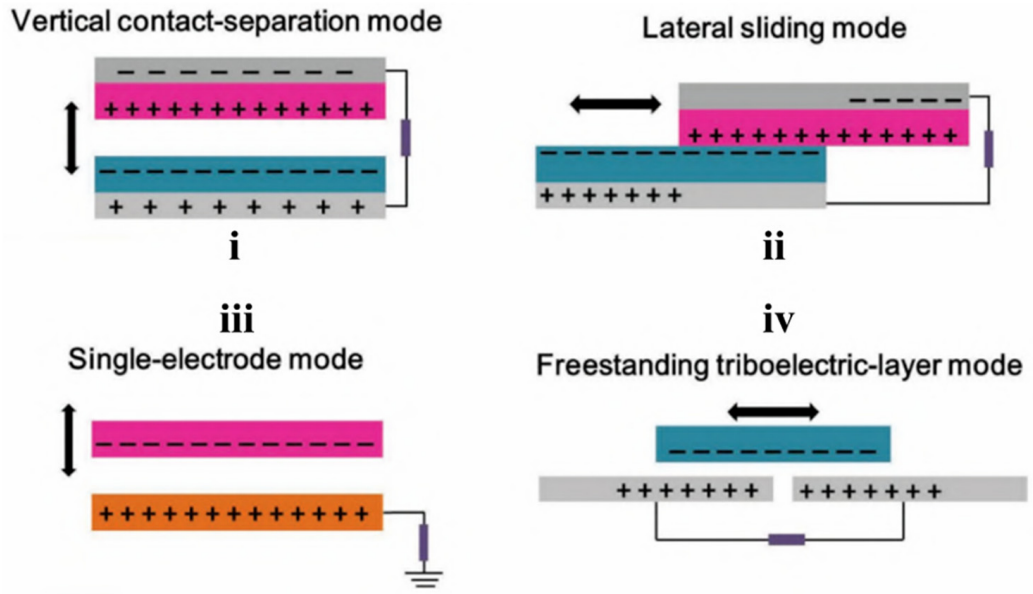

Figure 1. The Four Basic Working Modes of Triboelectric Nanogenerators [44]. The i–iv denote the four operational stages corresponding to different angular positions of the rotor. The "+" and "−" symbols represent the distribution of positive and negative triboelectric charges on the surfaces of the copper electrodes and FEP film, respectively.

The study introduces a self-powered silicon PIN photodetector system integrated with a ring-shaped TENG, emphasizing its notable advantages in cost-effectiveness and manufacturability. Experimental results demonstrate that the silicon PIN photodetector achieves excellent signal reception, while the ring-shaped TENG ensures stable and reliable power output. Compared to traditional TENG designs, the ring-shaped configuration provides enhanced stability, reducing fluctuations in power output. A key innovation of this system is its elimination of reliance on external power sources, addressing a common limitation of traditional photodetection systems. By integrating with an optical communica-

tion framework, this approach simplifies operational requirements and facilitates effective binary communication in emergency situations where conventional power is unavailable. The ring-shaped TENG is characterized by a straightforward design that can be efficiently constructed using inexpensive materials, including paper, Teflon tape, and copper foil. In contrast to conventional optical communication systems, the proposed self-powered system [45] eliminates the need for complex testing procedures and costly instrumentation, enhancing both usability and practicality [46–48]. This work provides meaningful insights into the development of self-powered optoelectronic devices, presenting substantial practical implications and promising potential for future innovation [48].

2. Experiment

2.1. Fabrication of Ring-Shaped TENG

We developed a ring-shaped TENG composed of an inner and an outer ring with different triboelectric materials (Figure 2). The 3D model was constructed using SolidWorks (Version 2022) software with a slot inside the inner ring which could be easily coupled with a servo motor to rotate efficiently. The design parameters of the bearing are as follows: the outer ring bore diameter is 52.6 mm, the outside diameter is 58 mm, and the width is 5.4 mm; the inner ring outside diameter is 52 mm, and the width is 5 mm. The inner ring is a rotor and outer ring is a stator. The stator inner surface has two equal-area copper foil electrodes attached to a 0.2 mm thick foam layer, to preserve conductivity and friction. In order to enhance friction, we attached an FEP film of size 0.1 mm thick to the outer surface of the stator and wrapped the entire stator in a nylon film. The resulting design led to a successfully produced ring-like TENG that can be used in future electrical tests and applications.

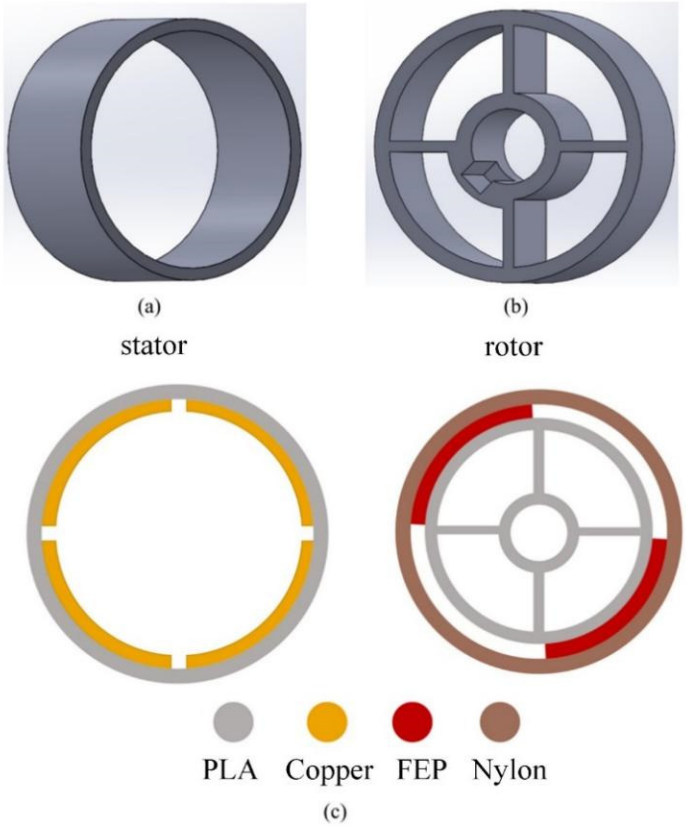

Figure 2. (**a**) Outer ring stator; (**b**) Inner ring rotor; (**c**) Schematic diagram of the planar structure of the ring TENG.

The working principle of the ring-shaped TENG can be described by the coupling of triboelectric effect and electrostatic induction, as illustrated in Figure 3. In Step 1 of the ring-shaped TENG, the FEP film on the rotor is fully aligned with a pair of copper electrodes on the stator, maximizing the contact area. However, due to the lack of relative sliding, no current is generated internally. At this point, negative charges migrate from the nylon surface to the FEP, and positive charges maintain a constant potential between the electrodes due to the static state. In Step 2, when the rotor rotates counterclockwise, relative sliding occurs between the FEP film and the copper foil electrodes, generating a large amount of triboelectric charges on the surface, and current begins to flow towards the load. As the rotation continues to Step 3, the FEP film is fully aligned with another pair of copper foil electrodes, reaching the maximum charge transfer. In Step 4, the direction of charge flow reverses until it returns to the fully aligned position of Step 1. With the rotor performing periodic counterclockwise motion, the ring-shaped TENG can continuously output an alternating current signal.

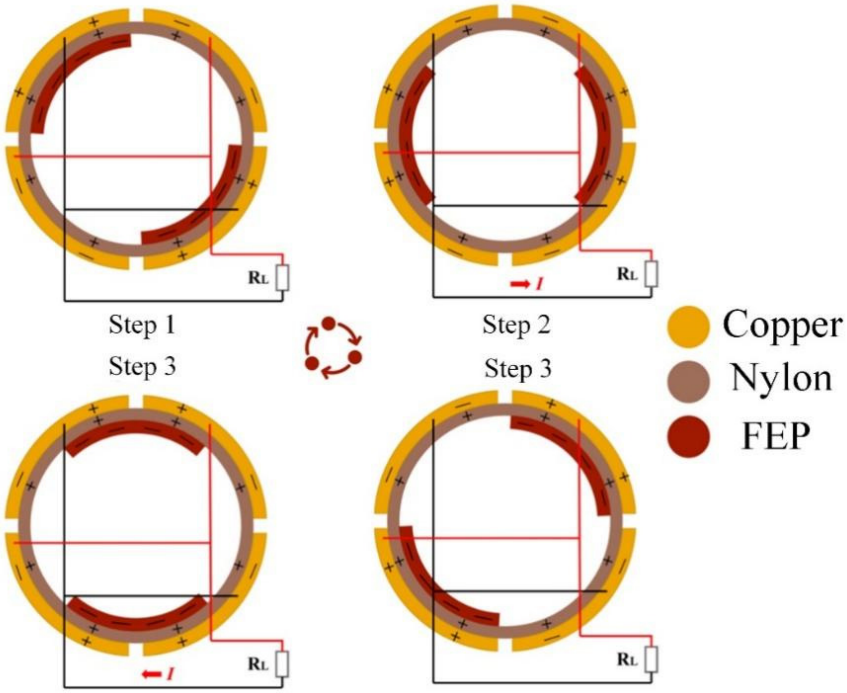

Figure 3. Working Principle of the Ring-shaped TENG. The "+" and "−" signs denote the distribution of positive and negative triboelectric charges, respectively.

To comprehensively demonstrate the operating mechanism of the ring-shaped TENG, COMSOL (Version 6.1) software was used to simulate its normal operation steps. Through this simulation process, the time evolution of the surface potential of the rotating TENG can be clearly observed. Figure 4a shows the potential distribution at a rotation angle of 0°, where the contact area between the friction material and the electrode is maximized. As the ring-shaped TENG rotates from this initial state, Figure 4b,d, respectively, show the potential distributions at 45°, 90°, and 135° angles. When the ring-shaped TENG rotates to 90°, the friction material completely overlaps with another set of electrodes, and further rotation forms a periodic operation. This cyclic process illustrates the complete working mechanism of the TENG, where the periodic changes in contact area and potential distribution together constitute the dynamic characteristics of the TENG during rotation.

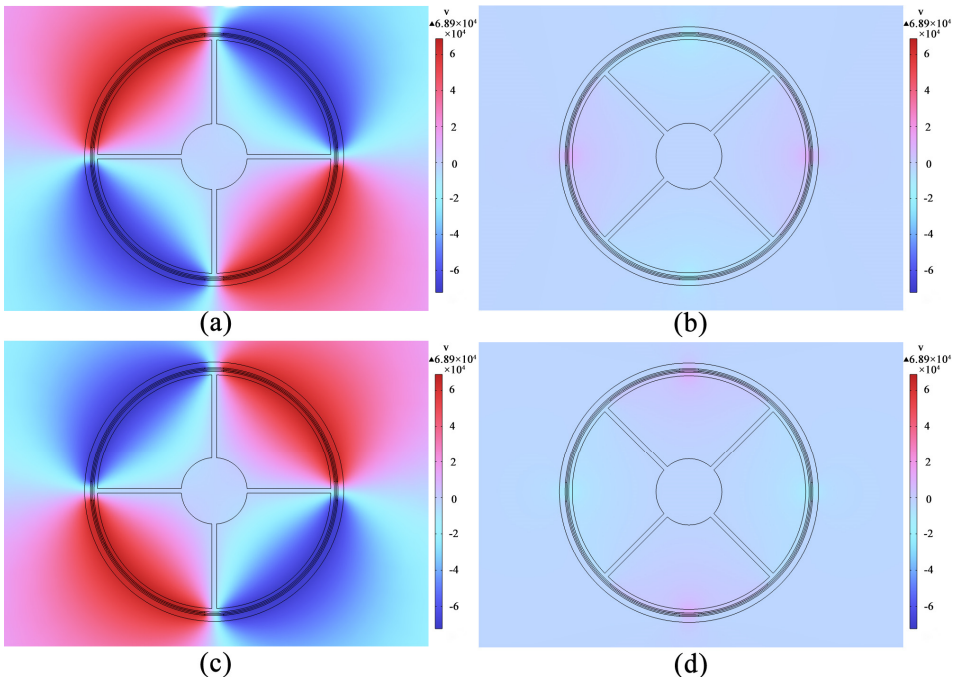

Figure 4. Simulation Results of Potential Distribution in the Ring-shaped TENG Operating States: (**a**) Rotation at 0°; (**b**) Rotation at 45°; (**c**) Rotation at 90°; (**d**) Rotation at 135°.

A series of output performance tests were conducted on the fabricated ring-shaped TENG (Figure 5). To ensure accuracy and repeatability of the tests, a servo motor was used to control the rotational speed of the TENG. A constant normal force of approximately 5N was applied via the mounting fixture of the servo motor to ensure consistent contact pressure during rotation. This setup, which maintains a consistent contact pressure, allows for the assessment of the TENG's electrical performance under stable mechanical conditions, thereby demonstrating its stability and suitability for driving photodetectors [49,50]. The voltage test results are presented in Figure 5a. As the rotational speed increased from 30 rpm to 360 rpm, the output voltage stabilized around 58 V, exhibiting minor fluctuations throughout the range. Although the output voltage amplitude remained stable, the density of the voltage pulse signals significantly increased with the rotational speed, exhibiting a linear relationship between the number of pulses per unit time and the rotational speed. This indicates that changes in rotational speed affect only the pulse interval and density, without significantly altering the output voltage. Figure 5b illustrates the relationship between output current and rotational speed. At lower rotational speeds, such as 30 rpm, the output current was measured at approximately 0.1 μA. As the speed increased, the current significantly rose, reaching a peak of 0.6 μA at 300 rpm. Beyond this speed, the current remained stable, indicating a positive correlation between output current and rotational speed only within a certain speed range. Figure 5c illustrates the relationship between output charge and rotational speed. As the speed increased, the charge stabilized at approximately 20 nC.

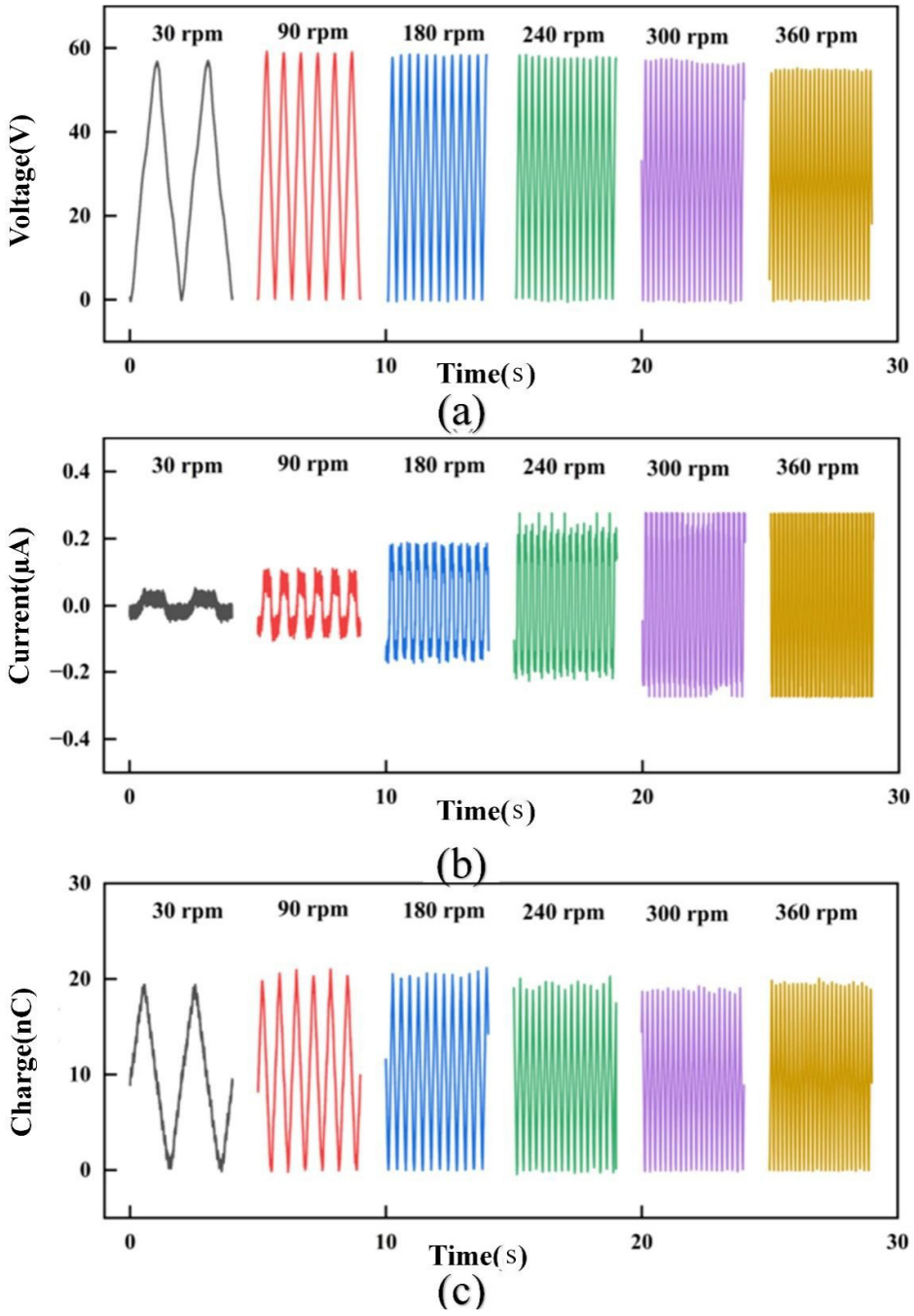

Figure 5. TENG output performance: (**a**) Voltage; (**b**) Current; (**c**) Charge.

2.2. Fabrication of Silicon PIN Photodetectors

This study utilizes square silicon PIN photodetectors, with a sensitive area side length of 25 mm and a thickness of 300 μm. This design helps to expand the acceptance range for incident light. The silicon PIN photodetectors operate under reverse bias voltage. Figure 6 illustrates the reverse bias current-voltage characteristics under dark conditions.

Figure 7 shows the magnified voltage response and recovery curves. The results indicate that the photodetector possesses excellent stability and repeatability, along with extremely fast response and recovery times. The dynamic performance of the silicon PIN photodetector was evaluated under pulsed light illumination. As shown in Figure 7, the device exhibited sharp and reproducible voltage transitions corresponding to the light switching cycles. When the light was turned on (Light ON), photo-generated carriers caused the output voltage to quickly rise from the dark baseline (approximately 0.4 V) to saturation

levels (about 7.3 V under 300 Lux), with a measured response time (τ_response) on the order of tens of milliseconds. When the light was turned off (Light OFF), the voltage similarly returned rapidly to the original baseline, with a recovery time (τ_recovery) comparable to the response time, indicating that the device has negligible persistent photoconductivity and is highly suitable for time-resolved detection. This fast and stable response aligns with the high-performance operational characteristics required for the subsequent TENG-driven optical communication system.

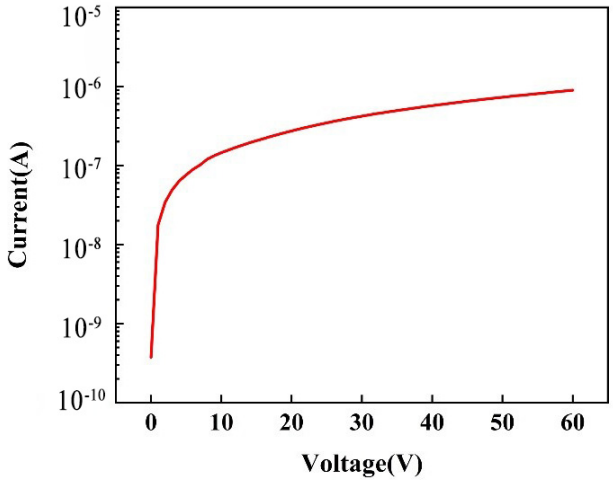

Figure 6. Reverse current-voltage characteristic curve of the silicon PIN photodetector.

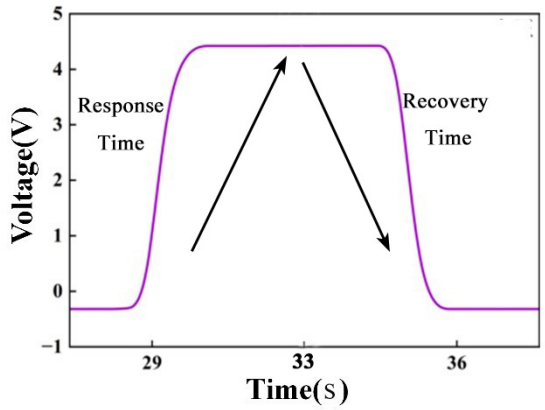

Figure 7. Voltage response of the silicon PIN photodetector subject to periodic light illumination, showing the response and recovery times.

2.3. Self-Powered Silicon PIN Detector System

In the traditional model, TENG-driven photodetectors typically rely on a direct parallel connection, where changes in the photodetector's resistance affect the TENG output voltage, thereby enabling light detection. However, this method suffers from stability issues. In contrast, the approach using a power management circuit first employs a ring-shaped TENG to harvest mechanical energy and convert it into pulsed alternating current. This alternating current signal is then rectified into a direct current signal via a rectifier bridge, and a capacitor is used for filtering and smoothing to eliminate pulsations. A Zener diode ensures the stability of the output voltage, allowing the photodetector to obtain a constant bias voltage under different mechanical operation conditions, thus achieving reliable light signal detection. Figure 8 presents a schematic diagram of the proposed self-powered photodetector circuit.

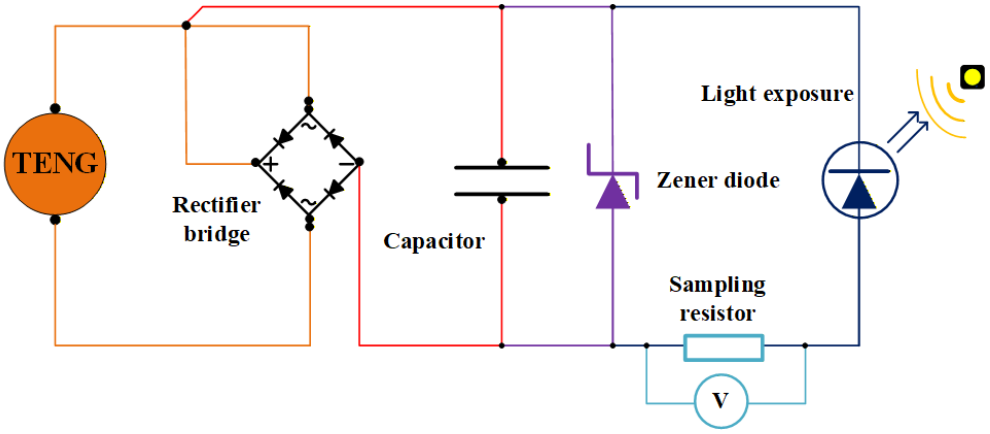

Figure 8. Circuit schematic of a self-powered photodetector.

Figure 9 presents the voltage response curves of the TENG-driven silicon PIN photodetector to varying light intensities at different rotational speeds, with a sampling resistor of 5 MΩ. The selection of a 5 MΩ sampling resistor represents a balanced trade-off between sensitivity and detection range. Based on experimental tests of impedance matching using 1, 2, and 5 MΩ resistors, 5 MΩ was chosen as the final value. Higher resistors increase voltage sensitivity but narrow the detectable range, while lower resistors extend the range at the cost of reduced sensitivity. As shown in Figure 9a, when the ring-shaped TENG is set to a rotational speed of 30 rpm and is in a no-light condition, the system's voltage output is 0.4 V. As the light intensity increases to 300 Lux, the system's output voltage rises stepwise, saturating at 7.3 V at 300 Lux and remaining unchanged with further increases in light intensity. When the light intensity is constant, the system output becomes a stable DC signal, with minor ripple signals appearing across the sampling resistor. Figure 9b–f illustrate the performance at rotational speeds ranging from 90 rpm to 360 rpm. By comparing Figure 9a–f, it is evident that the proposed TENG-driven silicon PIN photodetector, based on a power management circuit, exhibits output voltage that is nearly unaffected by rotational speed under the same light intensity, demonstrating excellent stability in the output voltage.

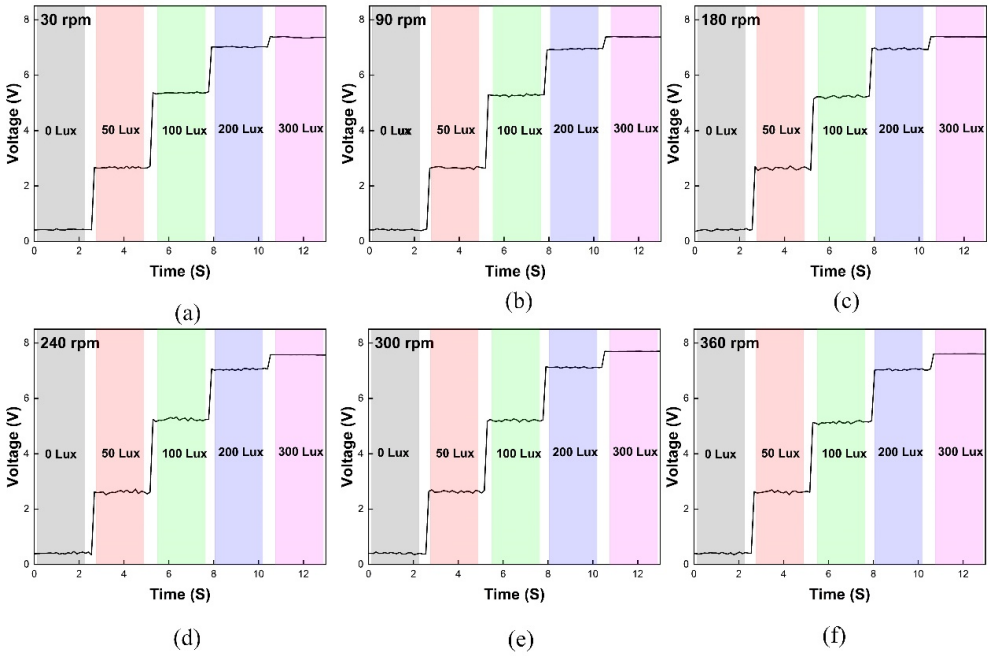

Figure 9. Voltage response curves of the TENG-driven photodetector to different light intensities at various rotational speeds: (**a**) 30 rpm; (**b**) 90 rpm; (**c**) 180 rpm; (**d**) 240 rpm; (**e**) 300 rpm; (**f**) 360 rpm.

3. Results and Discussion

The study proposes an optical communication system based on a triboelectric nanogenerator (TENG), with the specific working principle illustrated in Figure 10. This system is suitable for applications where power and infrastructure are limited, such as emergency signal transmission during disasters [51], electromagnetic interference-free communication in sensitive environments [52,53], and event-driven alerts in IoT networks [54]. Its self-powered feature and simple operation (pressing Morse code with a finger) make it a practical tool for rescue operations, confidential communication, and education, especially when traditional systems fail [55]. The hardware of the TENG-driven optical communication system is primarily composed of two main units: the signal transmission unit and the signal reception unit. The signal receiving unit consists of a TENG-driven silicon PIN photodetector powered by a rotating TENG, which has demonstrated high sensitivity to optical signals in experiments. Light-blocking measures were employed in the experiments to eliminate background light interference. The signal transmission unit consists of three finger-press TENGs (labeled TENG 1 to TENG 3) and a commercially available LED. The system operates without requiring an additional DC power source or complex modulation circuits, as the LED is driven to emit light solely by finger pressing. Due to the different friction layer areas of TENG 1 to 3, their output characteristics (voltage and current) vary significantly. In the experiments, pressing different TENGs generated different electrical signals, resulting in varying LED light intensities. The TENG-driven silicon PIN photodetector in the signal receiving unit can sense and convert these different light intensities. By using predefined coding rules and LabView (Version 2024 Q3) programming software, the computer can accurately decode and visualize the information transmitted by the signal-transmitting unit.

Based on the test results shown in Figures 11–13, variations in the peak feedback signals of different TENGs across different testers are observed. For example, for TENG 1, Tester 1's peak feedback signal ranges from 6.0 to 6.5 V, Tester 2's from 6.2 to 6.6 V, and Tester 3's from 6.3 to 6.8 V. Similar fluctuations are also noted for TENG 2 and TENG 3. However, the overall variation in peak feedback signals among testers is not substantial.

These results suggest that although there are slight differences in feedback signal results for the same TENG across different operators, the overall trend remains consistent. It further demonstrates that the signal receiving unit exhibits high stability and reliability in the output feedback signals of the TENG, ensuring accuracy across different testers. Consequently, it can be concluded that the system's reliability has been effectively validated.

Based on the analysis of the results, it can be concluded that although the electrical signals generated by the TENG exhibit some variability during pressing by different operators, the overall trend indicates that the peak values of the signals remain within a relatively stable range. Specifically, the peak feedback signal of TENG 1 ranges from 6.0 to 7.0 V, TENG 2 from 5.0 to 6.0 V, and TENG 3 from 4.7 to 5.0 V. This shows that the signals generated by TENG 1 through TENG 3 maintain a stable range, with no overlap between them, effectively eliminating the possibility of signal interference.

To ensure that the signal transmission unit can accurately represent Morse code and achieve clear communication, this chapter proposes a multi-threshold scheme. According to the feedback signal statistics shown in Table 1, the signal generated by TENG 1 corresponds to the logical signal 1, with a peak range of 6.0 to 7.0 V; TENG 2 corresponds to the logical signal 0, with a peak range of 5.0 to 6.0 V; and TENG 3 corresponds to the pause signal, with a peak range of 4.7 to 5.0 V. The design of this multi-threshold scheme aims to ensure the accurate transmission of Morse code and semantic clarity, thereby improving the reliability and accuracy of the system.

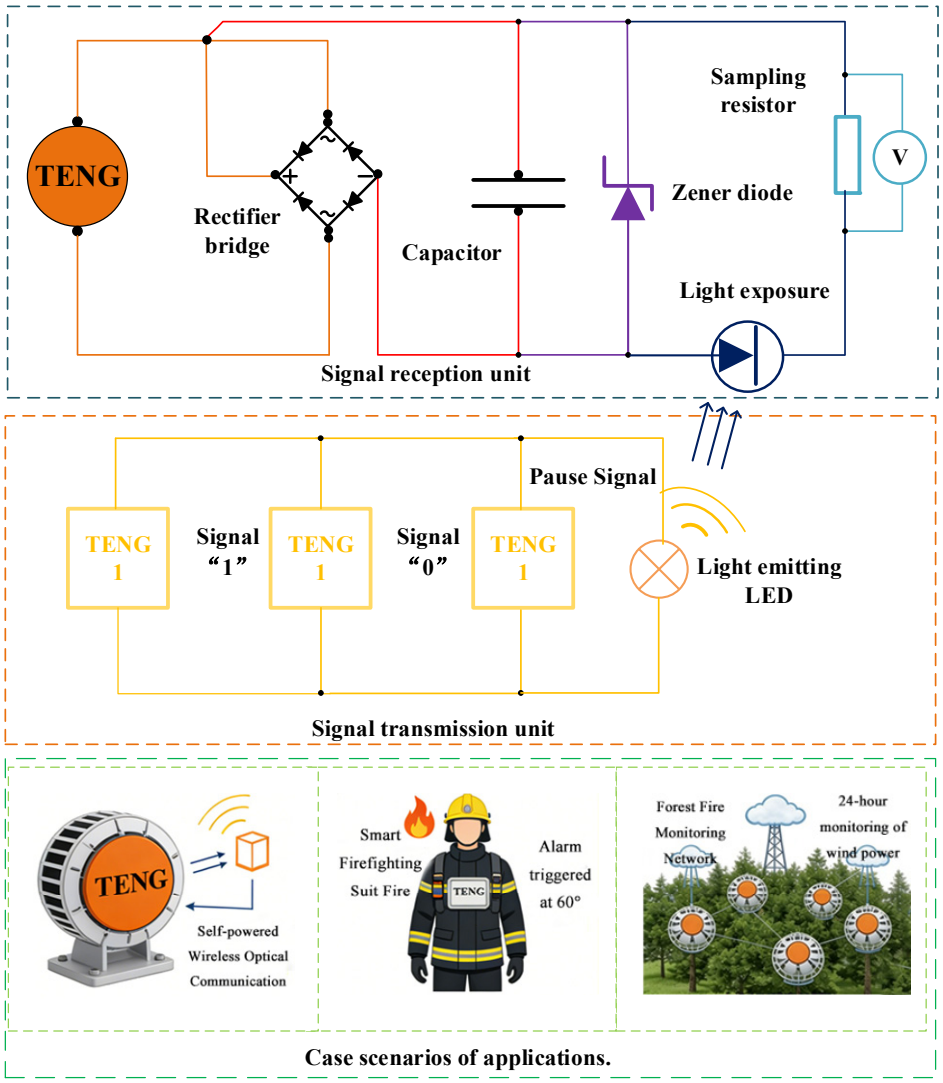

Figure 10. Schematic diagram of TENG-driven optical communication circuit.

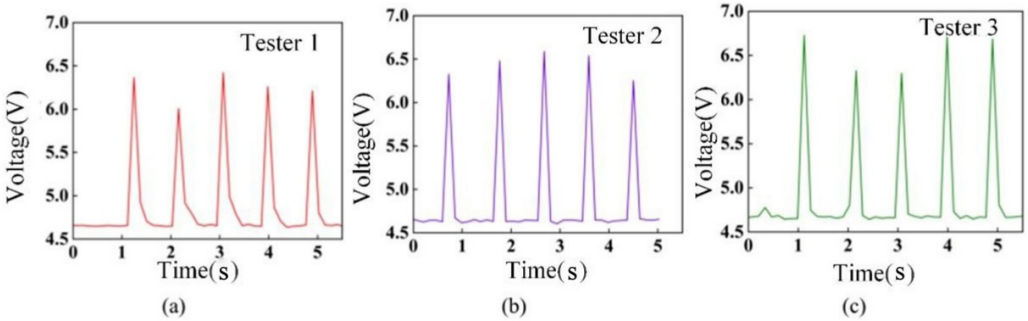

Figure 11. Results of TENG 1 Testing: (**a**) Operator 1, (**b**) Operator 2, and (**c**) Operator 3.

Table 1. Feedback signal statistics of TENG 1∼3.

TENG's Serial Number	The Range of the Peak Signal's Magnitude	Corresponding Logical Signal
TENG 1	6.0∼7.0	1
TENG 2	5.0∼6.0	0
TENG 3	4.7∼5.0	pause

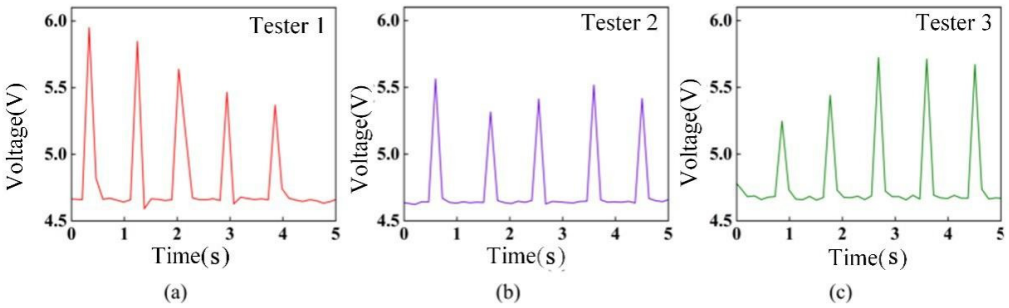

Figure 12. Results of TENG 2 Testing: (**a**) Operator 1, (**b**) Operator 2, and (**c**) Operator 3.

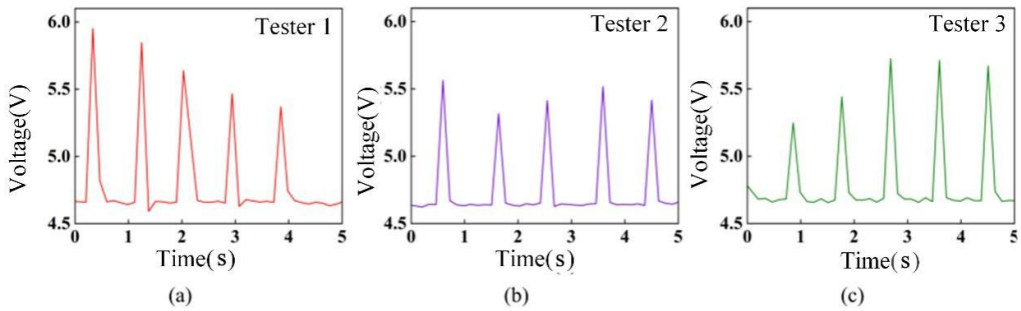

Figure 13. Results of TENG 3 Testing: (**a**) Operator 1, (**b**) Operator 2, and (**c**) Operator 3.

After completing the system design, the supporting LabView (Version 2024 Q3) software was developed to process and visualize the transmitted information. Subsequently, a comprehensive system test was conducted. As depicted in Figure 14, the experimenters simulated a scenario that required urgent assistance and transmitted "SOS" following Morse code rules. The signal receiving unit effectively detected the information and converted the optical signal into an electrical signal [56]. The signal processing unit then decoded and translated the message, which was displayed on the LabView software interface, resulting in successful communication. Figure 15 illustrates the visualization interface of another test result. These tests effectively confirmed the reliability and efficiency of the TENG-driven optical communication system [57].

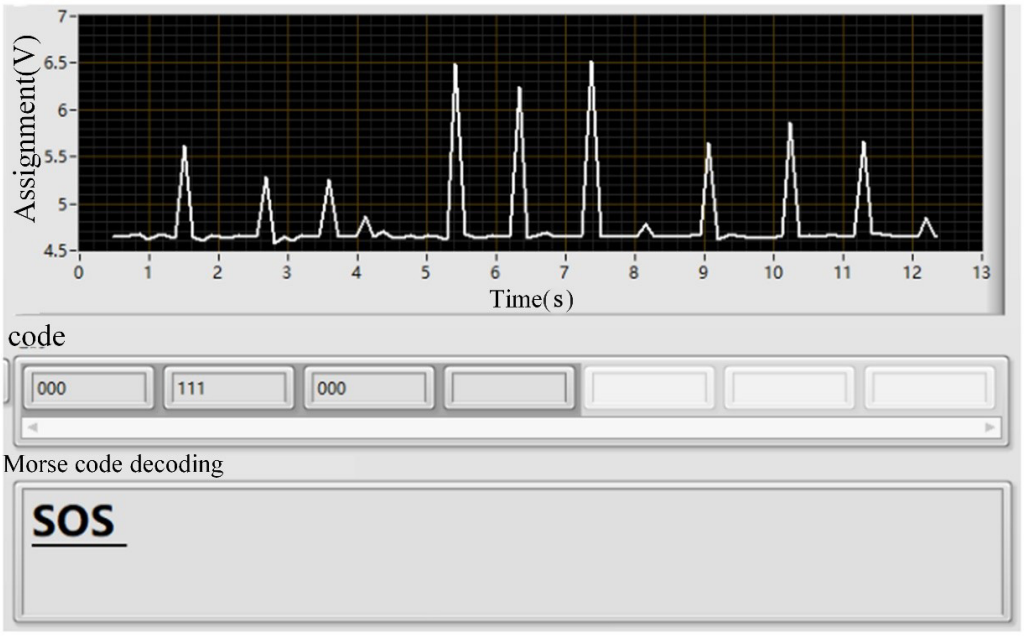

Figure 14. Results of Sending "SOS" Test.

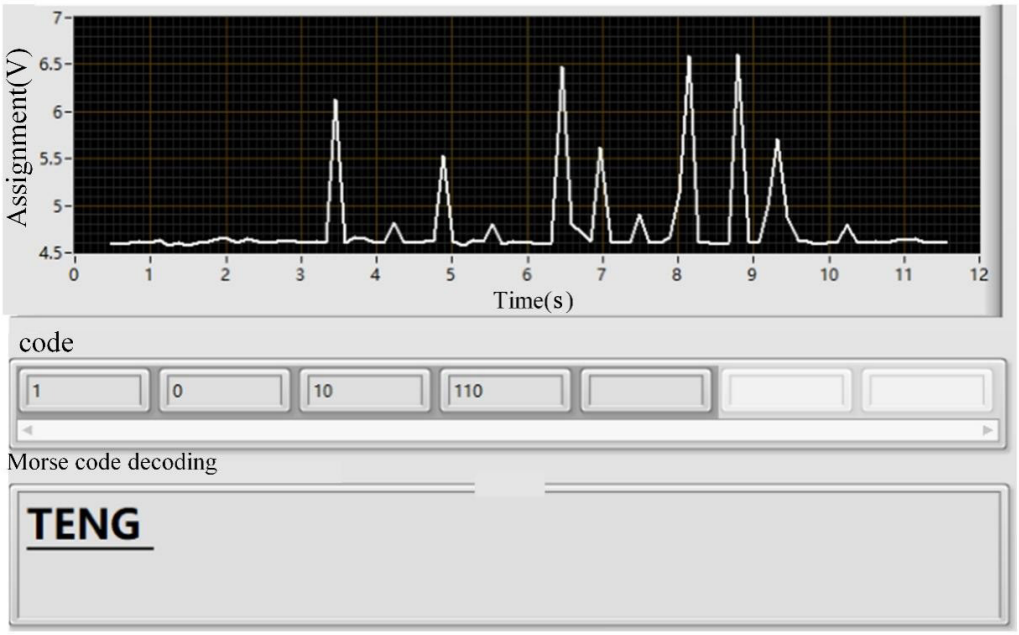

Figure 15. Results of Sending "TENG" Test.

4. Conclusions

In this study, we combined a triboelectric nanogenerator (TENG) with a silicon PIN photodetector to propose a TENG-driven silicon PIN photodetector based on a ring-shaped TENG. The detector remained stable despite changes in TENG rotational speed, addressing the issue of traditional TENG-driven photodetectors being affected by operational conditions. Using the TENG-driven silicon PIN photodetector as the receiving unit, we constructed a TENG-driven optical communication system by integrating a finger-press TENG and a commercial LED, achieving Morse code transmission and verifying the system's reliability and efficiency. This study presents a novel solution to the instability of traditional TENG-driven photodetectors, reduces reliance on conventional power sources, and introduces an innovative self-powered communication method that is particularly suitable for emergency scenarios where traditional power sources are unavailable [58]. This system is suitable for mountain rescue in emergencies, sending distress signals at sea, and communication during power outages in smart buildings [59]. Its self-powered feature reduces dependence on batteries, and the simple finger-press operation allows untrained users to deploy it quickly.

Author Contributions: Methodology, D.Y., R.Y. and Z.Z.; Validation, J.W., M.Z., H.L. and L.W.; Writing—original draft, D.Y.; Supervision, J.W., L.W., R.Y. and Z.Z. All authors have read and agreed to the published version of the manuscript.

Funding: This paper is supported by Key Laboratory of Intelligent Rehabilitation and Barrier-free for the Disabled (Changchun University), Ministry of Education (2024KFJJ006), National Natural Science Foundation of China (grant nos.62406260), the New Chongqing Youth Innovation Talent Project (CSTB2024NSCQ-QCXMX0072), Beibei District scientific research project (2025zzcxyj-07) and the Science and Technology Research Program of Chongqing Municipal Education Commission (Grant No. KJZD-K202500202).

Data Availability Statement: The original contributions presented in this study are included in the article. Further inquiries can be directed to the corresponding author.

Acknowledgments: The authors sincerely thank Bao Li for his significant contribution to the collection and processing of the experimental data.

Conflicts of Interest: The authors declare no conflict of interest.

References

1. Li, S.; Xu, L.D.; Zhao, S. The internet of things: A survey. *Inf. Syst. Front.* **2015**, *17*, 243–259. [CrossRef]
2. Park, K.S.; Park, J.M.; Yoon, Y.S.; Koo, J.G.; Kim, B.W.; Yoon, C.J.; No, K.S. Effects of the resistivity and crystal orientation of the silicon PIN detector on the dark current and radiation response characteristics. In Proceedings of the 2006 IEEE Nuclear Science Symposium Conference Record, San Diego, CA, USA, 29 October–4 November 2006; IEEE: Piscataway, NJ, USA, 2006; Volume 2, pp. 1068–1072.
3. Zhang, Z.; Yu, M.; Zhu, Z.; Wang, H.; Huang, Y.; Jin, Y. Fabrication of 1.5 mm thickness silicon pin fast neutron detector with guard ring structure. In Proceedings of the 2016 China Semiconductor Technology International Conference (CSTIC), Shanghai, China, 13–14 March 2016; IEEE: Piscataway, NJ, USA, 2016; Volume 1–3.
4. Rosenfeld, A.B.; Yudelev, M.; Lerch, M.L.F.; Cornelius, I.; Griffin, P.; Perevertailo, V.L.; Anokhin, I.E.; Zinets, O.S.; Khivrich, V.I.; Pinkovskaya, M.; et al. Neutron dosimetry with planar silicon pin diodes. *IEEE Trans. Nucl. Sci.* **2003**, *50*, 2367–2372. [CrossRef]
5. Liu, C.C.; Yu, M.; Fan, C.; Yang, F.D.; Zhou, C.Z.; Wang, J.Y.; Jin, Y.F. New PIN diode structure for neutron dose measurement. *J. Instrum.* **2012**, *7*, 08019. [CrossRef]
6. Zhou, C.; Zhao, J.; Xiao, W. PIN silicon diode fast neutron detector. *Radiat. Prot. Dosim.* **2005**, *117*, 365–368. [CrossRef]
7. Wang, P.; Tian, D.; Wang, S.; Yu, M.; Jin, Y. Research on the structure of ultrathin Si PIN detector. In Proceedings of the 8th Annual IEEE International Conference on Nano/Micro Engineered and Molecular Systems, Suzhou, China, 7–10 April 2013; IEEE: Piscataway, NJ, USA, 2013; pp. 629–632.
8. Liu, H.-Z.; Yu, M.; Shi, B.-H.; Qi, L.; Wang, S.-N.; Hu, A.-Q.; Du, H.; Wang, J.-Y.; Jin, Y.-F.; Yang, B. Study on geometry of silicon PIN radiation detector for breakdown voltage improvement. *Int. J. Nanotechnol.* **2015**, *12*, 753–760. [CrossRef]
9. Soref, R.A. Silicon-based optoelectronics. *Proc. IEEE* **1993**, *81*, 1687–1706. [CrossRef]
10. Jalali, B.; Yegnanarayanan, S.; Yoon, T.; Yoshimoto, T.; Rendina, I.; Coppinger, F. Advances in silicon-on-insulator optoelectronics. *IEEE J. Sel. Top. Quantum Electron.* **1998**, *4*, 938–947. [CrossRef]
11. Canham, L.T.; Cox, T.I.; Loni, A.; Simons, A.J. Progress towards silicon optoelectronics using porous silicon technology. *Appl. Surf. Sci.* **1996**, *102*, 436–441. [CrossRef]
12. Liu, J.; Camacho-Aguilera, R.; Bessette, J.T.; Sun, X.C.; Wang, X.X.; Cai, Y.; Kimerling, L.C.; Michel, J. Ge-on-Si optoelectronics. *Thin Solid Film.* **2012**, *520*, 3354–3360. [CrossRef]
13. Youngblood, N.; Li, M. Integration of 2D materials on a silicon photonics platform for optoelectronics applications. *Nanophotonics* **2017**, *6*, 1205–1218. [CrossRef]
14. Douhan, R.; Lozovoy, K.; Kokhanenko, A.; DeebORCID, H.; Dirko, V.; Khomyakova, K. Recent advances in Si-compatible nanostructured photodetectors. *Technologies* **2023**, *11*, 17. [CrossRef]
15. Jiang, H.; Wang, M.; Fu, J.; Li, Z.; Shaikh, M.S.; Li, Y.; Nie, C.; Sun, F.; Tang, L.; Yang, J.; et al. Ultrahigh photogain short-wave infrared detectors enabled by integrating graphene and hyperdoped silicon. *ACS Nano* **2022**, *16*, 12777–12785. [CrossRef] [PubMed]
16. Jiang, H.; Wei, J.; Sun, F.; Nie, C.; Fu, J.; Shi, H.; Sun, J.; Wei, X.; Qiu, C. Enhanced photogating effect in graphene photodetectors via potential fluctuation engineering. *ACS Nano* **2022**, *16*, 4458–4466. [CrossRef] [PubMed]
17. Fu, J.; Guo, Z.; Nie, C.; Sun, F.; Li, G.; Feng, S.; Wei, X. Schottky infrared detectors with optically tunable barriers beyond the internal photoemission limit. *Innovation* **2024**, *5*, 100600.
18. Fu, J.; Nie, C.; Sun, F.; Li, G.; Shi, H.; Wei, X. Bionic visual-audio photodetectors with in-sensor perception and preprocessing. *Sci. Adv.* **2024**, *10*, eadk8199. [CrossRef]
19. Cheng, T.; Shao, J.; Wang, Z.L. Triboelectric nanogenerators. *Nat. Rev. Methods Primers* **2023**, *3*, 39. [CrossRef]
20. Yadav, P.; Sahay, K.; Verma, A.; Maurya, D.K.; Yadav, B.C. Applications of multifunctional triboelectric nanogenerator (TENG) devices: Materials and prospects. *Sustain. Energy Fuels* **2023**, *7*, 3796–3831. [CrossRef]
21. Wang, Z.L.; Lin, L.; Chen, J.; Niu, S.M.; Zi, Y.L. Triboelectric nanogenerator: Vertical contact-separation mode. In *Triboelectric Nanogenerators*; Springer International Publishing: Cham, Switzerland, 2016; pp. 23–47.
22. Fan, F.-R.; Tian, Z.-Q.; Wang, Z.L. Flexible triboelectric generator. *Nano Energy* **2012**, *1*, 328–334. [CrossRef]
23. Wang, S.; Lin, L.; Wang, Z.L. Nanoscale triboelectric-effect-enabled energy conversion for sustainably powering portable electronics. *Nano Lett.* **2012**, *12*, 6339–6346. [CrossRef]
24. Yang, Y.; Lin, L.; Zhang, Y.; Jing, Q.; Hou, T.-C.; Wang, Z. Self-powered magnetic sensor based on a triboelectric nanogenerator. *ACS Nano* **2012**, *6*, 10378–10383. [CrossRef]
25. Bairagi, S.; Islam, S.; Kumar, C.; Babu, A.; Aliyana, A.; Stylios, G.; Pillai, S.C.; Mulvihill, D.M. Wearable nanocomposite textile-based piezoelectric and triboelectric nanogenerators: Progress and perspectives. *Nano Energy* **2023**, *118*, 108962. [CrossRef]
26. Huang, K.; Zhou, Y.; Zhang, Z.; Zhang, H.; Lü, C.; Luo, J.; Shen, L. A real-time quantitative acceleration monitoring method based on triboelectric nanogenerator for bridge cable vibration. *Nano Energy* **2023**, *118*, 108960. [CrossRef]
27. Wang, T.; Wang, C.; Zeng, Q.; Gu, G.; Wang, X.; Cheng, G.; Du, Z. A real-time, self-powered wireless pressure sensing system with efficient coupling energy harvester, sensing, and communication modules. *Nano Energy* **2024**, *125*, 109533.

28. Zhang, W.; Gu, G.; Qin, H.; Li, S.; Shang, W.; Wang, T.; Zhang, B.; Cui, P.; Guo, J.; Yang, F.; et al. Measuring the actual voltage of a triboelectric nanogenerator using the non-grounded method. *Nano Energy* **2020**, *77*, 105108. [CrossRef]
29. Ning, H.; Zhou, W.; Tuo, L.; Liang, C.; Chen, C.; Li, S.; Qu, H.; Wan, L.; Liu, G. Tensegrity triboelectric nanogenerator for broadband-blue energy harvesting in all-sea areas. *Nano Energy* **2023**, *117*, 108906.
30. Liu, J.; Zhou, L.; Gao, Y.; Yang, P.; Liu, D.; Qiao, W.; Zhang, B.; Zhao, Z.; Wang, Z.; Wang, J. Achieving Ultra-High Voltage (≈10 kV) Triboelectric Nanogenerators. *Adv. Energy Mater.* **2023**, *13*, 2300410. [CrossRef]
31. He, L.; Zhang, C.; Zhang, B.; Gao, Y.; Yuan, W.; Li, X.; Zhou, L.; Zhao, Z.; Wang, Z.; Wang, J. A high-output silk-based triboelectric nanogenerator with durability and humidity resistance. *Nano Energy* **2023**, *108*, 108244. [CrossRef]
32. Xia, X.; Zhou, Z.; Shang, Y.; Yang, Y.; Zi, Y. Metallic glass-based triboelectric nanogenerators. *Nat. Commun.* **2023**, *14*, 1023. [CrossRef] [PubMed]
33. Liu, D.; Gao, Y.; Zhou, L.; Wang, J.; Wang, Z. Recent advances in high-performance triboelectric nanogenerators. *Nano Res.* **2023**, *16*, 11698–117179. [CrossRef]
34. Yang, Y.; Guo, X.; Zhu, M.; Sun, Z.; Zhang, Z.; He, T.; Lee, C. Triboelectric nanogenerator enabled wearable sensors and electronics for sustainable internet of things integrated green earth. *Adv. Energy Mater.* **2023**, *13*, 2203040.
35. Gai, Y.; Jiang, Y.; Li, Z. Advances in health rehabilitation devices based on triboelectric nanogenerators. *Nano Energy* **2023**, *116*, 108787. [CrossRef]
36. Qian, J.; Kim, D.-S.; Lee, D.-W. On-vehicle triboelectric nanogenerator enabled self-powered sensor for tire pressure monitoring. *Nano Energy* **2018**, *49*, 126–136.
37. Rasel, M.S.; Maharjan, P.; Salauddin, M.; Rahman, M.T.; Cho, H.O.; Kim, J.W.; Park, J.Y. An impedance tunable and highly efficient triboelectric nanogenerator for large-scale, ultra-sensitive pressure sensing applications. *Nano Energy* **2018**, *49*, 603–613.
38. Gao, X.; Huang, M.; Zou, G.; Li, X.; Wang, Y. Self-powered vibration sensor based on the coupling of dual-mode triboelectric nanogenerator and non-contact electromagnetic generator. *Nano Energy* **2023**, *111*, 108356. [CrossRef]
39. Fang, L.; Zheng, Q.; Hou, W.; Zheng, L.; Li, H. A self-powered vibration sensor based on the coupling of triboelectric nanogenerator and electromagnetic generator. *Nano Energy* **2022**, *97*, 107164. [CrossRef]
40. Yao, Y.; Zhou, Z.; Wang, K.; Liu, Y.; Lu, X.; Cheng, T. Arc-shaped flutter-driven wind speed sensor based on triboelectric nanogenerator for unmanned aerial vehicle. *Nano Energy* **2022**, *104*, 107871. [CrossRef]
41. Yu, X.; Fu, S.; Zuo, X.; Zeng, J.; Shan, C.; He, W.; Li, W.; Hu, C. Moisture resistant and stable wireless wind speed sensing system based on triboelectric nanogenerator with charge-excitation strategy. *Adv. Funct. Mater.* **2022**, *32*, 2207498.
42. Zhao, K.; Gu, G.; Zhang, Y.; Zhang, B.; Yang, F.; Zhao, L.; Zheng, M.; Cheng, G.; Du, Z. The self-powered CO_2 gas sensor based on gas discharge induced by triboelectric nanogenerator. *Nano Energy* **2018**, *53*, 898–905. [CrossRef]
43. Liu, T.; Cui, J.; Zheng, Y.; Bai, S.; Hao, C.; Xue, C. A self-powered inert-gas sensor based on gas ionization driven by a triboelectric nanogenerator. *Nano Energy* **2023**, *106*, 108083. [CrossRef]
44. Zheng, Q.; Shi, B.; Li, Z.; Wang, Z. Recent progress on piezoelectric and triboelectric energy harvesters in biomedical systems. *Adv. Sci.* **2017**, *4*, 1700029. [CrossRef]
45. Wang, T.; Gu, G.; Shang, W.; Gan, J.; Zhang, W.; Luo, H.; Zhang, B.; Cui, P.; Guo, J.; Yang, F.; et al. A self-powered photodetector using a pulsed triboelectric nanogenerator for actual working environments with random mechanical stimuli. *Nano Energy* **2021**, *90*, 106518. [CrossRef]
46. Alam, M.M.; Crispin, X. The past, present, and future of piezoelectric fluoropolymers: Towards efficient and robust wearable nanogenerators. *Nano Res. Energy* **2023**, *2*, e9120076. [CrossRef]
47. Guo, X.; He, J.; Zheng, Y.; Wu, J.; Pan, C.; Zi, Y.; Cui, H.; Li, X. High-performance triboelectric nanogenerator based on theoretical analysis and ferroelectric nanocomposites and its high-voltage applications. *Nano Res. Energy* **2023**, *2*, e9120074.
48. Liu, L.; Guo, X.; Lee, C. Promoting smart cities into the 5G era with multi-field internet of things (IoT) applications powered with advanced mechanical energy harvesters. *Nano Energy* **2021**, *88*, 106304. [CrossRef]
49. Wang, J.; Xia, K.; Liu, J.; Li, T.; Zhao, X.; Shu, B.; Li, H.; Guo, J.; Yu, M.; Tang, W.; et al. Self-powered silicon PIN photoelectric detection system based on triboelectric nanogenerator. *Nano Energy* **2020**, *69*, 104461. [CrossRef]
50. Xu, Q.; Lu, Y.; Zhao, S.; Hu, L.; Jiang, Y.; Li, H.; Wang, Y.; Gao, H.; Li, Y.; Yuan, M.; et al. A wind vector detecting system based on triboelectric and photoelectric sensors for simultaneously monitoring wind speed and direction. *Nano Energy* **2021**, *89*, 106382. [CrossRef]
51. Liu, W.; Wang, X.; Song, Y.; Cao, R.; Wang, L.; Yan, Z.; Shan, G. Self-powered forest fire alarm system based on impedance matching effect between triboelectric nanogenerator and thermosensitive sensor. *Nano Energy* **2020**, *73*, 104843. [CrossRef]
52. Gu, G.; Gu, G.; Shang, W.; Zhang, Z.; Zhang, W.; Wang, C.; Fang, D.; Cheng, G.; Du, Z. The self-powered agricultural sensing system with 1.7 km wireless multichannel signal transmission using a pulsed triboelectric nanogenerator of corn husk composite film. *Nano Energy* **2022**, *102*, 107699. [CrossRef]
53. Ding, W.; Wu, C.; Zi, Y.; Zou, H.; Wang, J.; Cheng, J.; Wang, A.C.; Wang, Z. Self-powered wireless optical transmission of mechanical agitation signals. *Nano Energy* **2018**, *47*, 566–572. [CrossRef]

54. Pandey, P.; Thapa, K.; Ojha, G.P.; Seo, M.K.; Shin, K.H.; Kim, S.H.; Sohn, J.I. Metal-organic frameworks-based triboelectric nanogenerator powered visible light communication system for wireless human machine interactions. *Chem. Eng. J.* **2023**, *452*, 139209.
55. Wang, Z.L. From contact electrification to triboelectric nanogenerators. *Rep. Prog. Phys.* **2021**, *84*, 096502. [CrossRef]
56. Zhao, X.; Liu, L.; Yin, D.; Su, Y.; Hu, T.; Zheng, Y.; Yang, T.; Shi, Q.; Tao, K. A vehicle-to-everything (V2X) interaction system for intelligent transportation based on energy harvesting–sensing cooperation triboelectric nanogenerator. *ACS Appl. Electron. Mater.* **2025**, *7*, 7419–7431. [CrossRef]
57. Liu, L.; Zhao, X.; Hu, T.; Liang, F.; Guo, B.; Tao, K. Deep-learning-assisted self-powered wireless environmental monitoring system based on triboelectric nanogenerators with multiple sensing capabilities. *Nano Energy* **2024**, *132*, 110301. [CrossRef]
58. Su, Y.; Yin, D.; Zhao, X.; Hu, T.; Liu, L. Exploration of advanced applications of triboelectric nanogenerator-based self-powered sensors in the era of artificial intelligence. *Sensors* **2025**, *25*, 2520. [CrossRef] [PubMed]
59. Liu, L.; Hu, T.; Zhao, X.; Su, Y.; Yin, D.; Lee, C.; Wang, Z. Innovative smart gloves with phalanges-based triboelectric sensors as a dexterous teaching interface for embodied artificial intelligence. *Nano Energy* **2025**, *133*, 110491. [CrossRef]

Disclaimer/Publisher's Note: The statements, opinions and data contained in all publications are solely those of the individual author(s) and contributor(s) and not of MDPI and/or the editor(s). MDPI and/or the editor(s) disclaim responsibility for any injury to people or property resulting from any ideas, methods, instructions or products referred to in the content.